

# The detector response matrices of the burst and transient source experiment (BATSE) on the Compton Gamma Ray Observatory

Geoffrey N. Pendleton <sup>a,\*</sup>, William S. Paciesas <sup>a</sup>, Robert S. Mallozzi <sup>a</sup>, Tom M. Koshut <sup>a</sup>,  
Gerald J. Fishman <sup>b</sup>, Charles A. Meegan <sup>b</sup>, Robert B. Wilson <sup>b</sup>, John M. Horack <sup>b</sup>,  
John Patrick Lestrade <sup>c</sup>

<sup>a</sup> Department of Physics, University of Alabama in Huntsville, Huntsville, AL 35899, USA

<sup>b</sup> NASA / Marshall Space Flight Center, Huntsville, AL 35812, USA

<sup>c</sup> Department of Physics, Mississippi State University, Starkville, MS 39762, USA

Received 16 February 1995

## Abstract

The detector response matrices for the Burst And Transient Source Experiment (BATSE) on board the Compton Gamma Ray Observatory (CGRO) are described, including their creation and operation in data analysis. These response matrices are a detailed abstract representation of the gamma-ray detectors' operating characteristics that are needed for data analysis. They are constructed from an extensive set of calibration data coupled with a complex geometry electromagnetic cascade Monte Carlo simulation code. The calibration tests and simulation algorithm optimization are described. The characteristics of the BATSE detectors in the spacecraft environment are also described.

## 1. Introduction

Since the CGRO launch, April 5 1991, the BATSE [1,2] gamma-ray detectors have been used to study gamma-ray bursts [3] and other distant astrophysical objects [4,5], solar flares [6], and gamma-rays emitted in the upper atmosphere of the earth [7]. All of these studies rely on the use of an accurate model of the instrument performance. BATSE employs eight large area detectors (LADs) and eight spectroscopy detectors (SDs) to provide all sky monitoring capability. The detector response matrices (DRMs) are an abstract representation of the BATSE gamma-ray detectors' response characteristics. They are designed to convert background-subtracted source counts to incident photon spectra. They express the response in terms of the incident photon input energy, the measured detector output energy, and the angle between the detector normal and the source direction. The need for detailed separation of input and output energy became apparent when measurements of SN1987A and the Crab Nebula [8] were made using balloon-borne detectors similar to the BATSE detectors. Having the detector response expressed as a matrix of input vs. output energy with the off diagonal

terms explicitly included was necessary to perform spectral analysis accurately using the inverse matrix method.

The detector response matrices described here are also used by the BATSE data analysis software to locate gamma-ray bursts and other transient sources. Other uses include the spectral analysis of sources observed using the earth occultation technique, pulsed source location and spectral analysis as well as solar flare and upper atmosphere event location and spectral analysis. This paper outlines the procedures and tools used to create the DRMs and is intended to aid users of BATSE data and those attempting projects of similar subject and scope.

## 2. The detector simulation software

The physical kernel of the simulation section of this project is a version of the EGS software [9,10] that has been modified to include physical effects that are important to BATSE below 100 keV. The EGS code contains all the physics needed to simulate photoelectric absorption, Compton scattering, and pair production for photons. It also implements electron interaction processes including bremsstrahlung, annihilation, and multiple Coulomb scattering. In order to accurately represent the physics observed in the BATSE detectors, it is necessary to simulate the transport of photons that are usually emitted after a

\* Corresponding author. Tel. +1 205 544 3954, fax +1 205 544 5800, e-mail: pendleton@sslmor.msfc.nasa.gov.

photoelectric absorption, particularly for sodium iodide and lead, in the event that these X-rays leave the material without interacting. The photoelectric absorption section of the simulation code was modified to produce and transport the photons emitted when the atomic electrons drop down and occupy the K-shell orbits vacated during the photoelectric absorption. The energies and probabilities of emission for these photons were taken from Browne et al. [11]. This code package produces the total and differential photon and electron interaction cross sections for all elements and mixtures of elements over the energy range of interest here.

A complex geometry code was written specifically for the BATSE detector simulation. This code delineates the volumes of material that comprise the detector and its environment in which the electromagnetic interactions take place and transports the particles between volumes. Nested volume sets are organized in a hierarchy up to seven layers deep for the most complicated scenarios simulated. At each layer of the hierarchy the nearest neighbour volumes for each volume cell are stored as efficiently as possible. It is important to keep track of nearest neighbour volumes when the geometry involved contains thousands of volume cells; otherwise large amounts of computer time can be used up calculating what the next volume should be when a particle leaves one volume and enters another.

At each level in the volume hierarchy, translations and rotations can be performed on the volume elements. For example, the spectroscopy detector volumes are delineated by a set of concentric cylindrical shells contained within a rectangular box. This box is then translated to its proper position and rotated to its proper orientation with respect to the entire BATSE module. At a higher level the entire BATSE module is enclosed in a spherical shell that can be translated and rotated to any position in a test environment or on the corner of the CGRO spacecraft.

In order to test this algorithm effectively it is necessary to be conversant with a symbolic debugger and to have access to a 3D graphics package. The symbolic debugger is necessary to track the particles of the electromagnetic cascade through the geometry in order to work out the particle transport algorithms properly. Since this is a Monte Carlo code, there are virtually an infinite number of ways a photon history can be realized. Given the complicated geometry of this particular simulation the photon histories are each likely to be quite distinct, particularly at the end of their development. Therefore it is not possible to predict in advance all the cases that can be encountered. In some cases round off errors can cause problems, particularly for particles involved in grazing incidence intersections with curved surfaces. The symbolic debugger allows the algorithm designer to study the particular flow of control of the program in problem cases and to optimize the code to make it robust. A 3D graphics display tool is useful to observe the trajectories of particles to insure that the transfer between volumes proceeds correctly, particularly

when translation and rotation operators are applied between volumes. It is also important to verify the positioning of the detector elements in the simulation geometry. These two tools allow the algorithm designer to confidently construct and successfully test routines that are considerably more complex than the kind that can be worked out in complete detail in advance.

The type of algorithm that can be produced with this approach has trans-analytic properties since it produces results that cannot be obtained with a finite series of analytic equations executed in a fixed order. The fact that the algorithm has the capacity to select the sequence of calculations with virtually infinite variety allows it to probe new domains of problem solving inaccessible to conventional analytic techniques. This is generally true for Monte Carlo techniques and it is particularly true for a complex Monte Carlo code coupled to detailed geometry simulation.

An important feature of this algorithm is that if two large but finite sets of 100 keV photon histories are run through the simulation, and the energy deposition in a detector crystal is tabulated for each set, their energy deposition spectra will agree within statistical uncertainties even though the step by step development of each set of histories is markedly different. Hence this algorithm with virtually an infinite variety of distinct realizations produces results that converge in a well-limited way to the characteristic detector response of the instrument. This is, of course, exactly what happens in the actual test environment. It should also be noted that the final results of this program, the DRMs themselves, are of finite dynamic complexity. They are represented by a set of analytic equations and the evaluation of a particular DRM involves an equation evaluation sequence that is fixed.

Fig. 1 shows a diagram of a BATSE module compared to a computer generated outline of some of the volumes used in the Monte-Carlo simulation. The volumes in the BATSE module were determined from the engineering drawing, and reproduced in many cases with sub-millimeter accuracy.

The large area detector consists of NaK(Tl) crystal disk 25.4 cm in radius and 1.27 cm thick. The crystal is mounted on a quartz window 25.90 cm in radius and 1.905 cm thick. The NaI crystal is covered with a thin silicon pad and a 1 mm thick aluminum cover. This assembly is surrounded by an invar steel mounting ring. This crystal assembly is mounted on a truncated cone 30 cm deep whose inside surface is coated with a barium sulphate-based white reflecting paint. The crystal is viewed by three 12.7 cm diameter photomultiplier tubes (PMTs) mounted on a 19 cm radius base. The cone and base have a 0.86 g/cm<sup>2</sup> layer of lead which serves as passive shielding behind the crystal. On top of the lead is a 0.7 mm layer of tin to absorb lead fluorescence. In front of the LAD crystal is a polystyrene charged particle detector (CPD) 6.35 mm thick sandwiched between two aluminum hexel sheets 7 mm

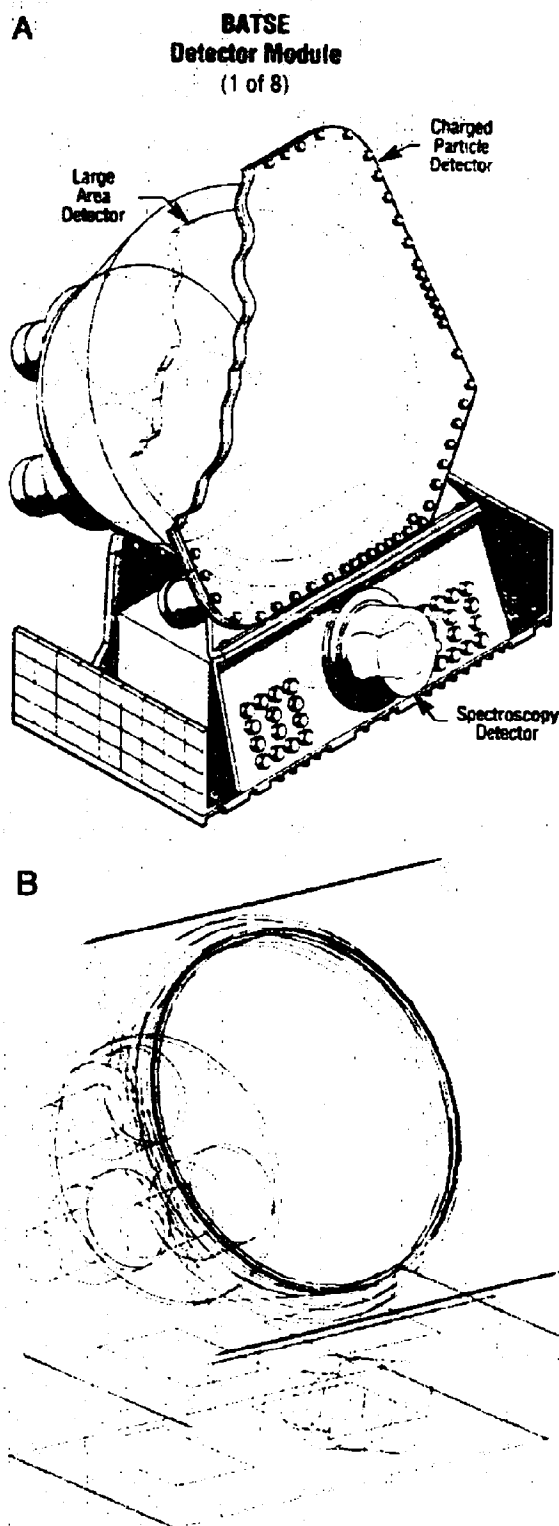


Fig. 1. Comparison of simulation and actual BATSE detector geometry. (a) is a diagram of the detector module and (b) is a computer generated diagram of key volumes employed in the Monte Carlo simulation.

thick. Around the edge of the LAD detector crystal between it and the CPD are numerous wire harness assemblies, mounting rings, the two CPD PMTs, and other smaller assemblies. This mass distribution is approximated by a series of concentric rings about the crystal assembly. The LAD response at large angles where this material is important was optimized using in flight solar flare data [12-14].

The spectroscopy detector consists of a 7.195 cm thick NaI(Tl) crystal 65.15 mm in radius. The sides of the detector are covered with 1.5 mm of silicon compound and 1.3 mm of aluminum. The top of the crystal has a 38.1 mm radius beryllium disk 1.27 mm thick over its center surrounded by an aluminum ring 0.68 mm thick with the silicone compound underneath it. The crystal is mounted on a quartz window 0.95 cm thick then mounted on a 5 in. PMT. A steel ring 0.95 cm thick and 1.26 cm high surrounds the base of the crystal assembly. This detector assembly is mounted in an aluminum plate whose mass and general dimensions are modeled in the simulation. The other objects surrounding the spectroscopy detector include the BATSE module base, the two radiators to either side, the BATSE power module and the detector electronics unit. All these objects are included in the simulation.

The specific results of the simulation of values for the detector model are the charged particle energy depositions collected in the detector crystals when photons interact there. When an individual photon is processed through the simulation algorithm, the energy depositions of all electrons produced in the electromagnetic cascade that occur within the detector crystal are summed to yield the total energy deposition for that photon. When an ensemble of monoenergetic photons are processed in this manner a set of deposited energies are produced that are referred to here as an energy deposition spectrum. When this spectrum is further processed to incorporate other important detector characteristics like the detector's energy resolution a detector response profile is produced. This response profile represents the characteristic response of the detector to an ensemble of photons at a particular energy.

### 3. Calibration of the simulation geometry using angular response and absolute efficiency test data

The accuracy of the simulations was optimized and verified by comparison of the simulation results with experimental test data, specifically the BATSE absolute efficiency and angular response test data. The optimized simulation results, combined with other parameters determined from instrument tests were used to construct the DRMs. In order to accurately interpret the results of the instrument tests, the simulations were run with the detector geometry imbedded in an accurate representation of the tests environment as allowable by the geometry software package.

The absolute efficiency tests were designed to verify the amplitude of each of BATSE's eight LAD and eight SD detectors response at a variety of energies. The relative efficiencies between detectors were measured as well as the energy resolution of each detector. The detector modules were placed on a table and various  $\gamma$ -ray emitting isotopes were exposed to the detectors. For the LAD measurements, these sources were placed 110 in. from the outer CPD surface along the detector axis. An aluminum support was used to hold the sources in place. It consisted primarily of  $\frac{1}{8}$  and  $\frac{1}{4}$  in. thick plates that did not absorb all the  $\gamma$ -rays that entered them. In this configuration about 0.4% of the  $\gamma$ -rays emitted isotropically at the source traveled directly to the LAD detector. A large fraction of the rest of the flux passed through or Compton scattered in the source holder and then Compton scattered from objects in the test room. Some of this scattered flux interacted in the detector as well. A fairly simple rectangular geometry was used to simulate the test environment. It was found that the scattered flux observed by the detectors was very sensitive to the positions of volumes of mass in the test environment when  $\gamma$ -rays above 100 keV were present. The magnitude of the scattered flux observed could be changed by a factor of 2 by moving mass elements around in the test environment. In order to simulate the scattered flux in this geometry accurately a geometry at least two orders of magnitude more complex than that used here would be necessary coupled with precise characterizations of the masses in the test room.

However for  $\gamma$ -rays above a couple hundred keV, the energy of the photons Compton scattered in the test environment differed significantly from the initial photon energy by the time they reached the detector. Hence the events that deposited the  $\gamma$ -ray source full energy for these  $\gamma$ -rays were due entirely to the 0.4% of the photons impinging directly on the detector. These events appear in the detector response profile as an approximately Gaussian feature centered on the full energy deposition value, referred to here as the photopeak of the response profile.

The absolute efficiency of the detectors could be verified with this photopeak data. The calculations for the 279 keV  $\gamma$ -rays of  $\text{Hg}^{203}$  are given as an example. In the experimental data, the number of 279 keV photons incident on the detector during a 393.2 min  $\text{Hg}^{203}$  exposure is calculated to be 1 400 000 photons with an error of approximately 5% due to the uncertainties in the source strength [15]. The photopeak counts were taken to be twice the number of counts on the high energy half of the photopeak. This technique was used in order to avoid having to cope with the contamination of the lower half of the photopeak by the non-photopeak components of the detector response profile. For the  $\text{Hg}^{203}$  279 keV line, in this way it was determined from the 553 800 of the 1 400 000 incident photons ended up in the photopeak.

In the simulation of the  $\text{Hg}^{203}$  exposure 4983 279 keV photons were directly incident on the detector crystal area.

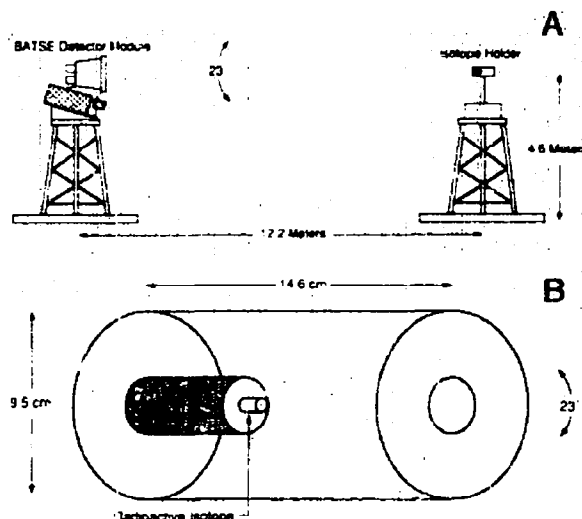


Fig. 2. The angular response test geometry. (a) shows the positioning of the detector module with respect to the source holder. (b) shows the collimator geometry for the radioactive sources used in the angular response test.

Of these 2010 ended up in the photopeak. To compare the Monte Carlo and experimental results one compares the ratio of the photons in the photopeak to the photons incident on the detector crystal. The experimental ratio of photopeak photons to directly incident photons is (from the two values given above)  $39.5\% \pm 5\%$ . The Monte Carlo ratio is  $40.3\% \pm 1\%$ . These results agree within errors indicating that the simulation is operating correctly.

The absolute efficiency at lower energies is verified by the simulations of measurements using isotopes that emit low and high energy gamma-rays simultaneously with well known ratios. The angular response test results shown in Fig. 4 demonstrate that the low energy absolute efficiency is well represented by the simulations since the simulated response to 32 and 80 keV photons is correct relative to the higher energy lines, as can be seen by the comparison of the Monte Carlo results to the laboratory measurements. In fact for photons with normal incidence below 150 keV the absolute efficiency is accurately described using a product of the detector geometric area, attenuation in the CPD, and absorption in the LAD.

The angular response test was designed to measure the detector response for photons at various incident angles, as well as the off diagonal components of the detector response. The geometry for this test is shown in Fig. 2a. In this geometry, a collimating source holder was used to minimize the scattering flux observed by the detector. Both the source holder and detector were positioned 4.6 m above the floor in order to avoid scattering from there. The limited complexity of the source holder made it possible to simulate it accurately. The geometry for the source holder is shown in Fig. 2b. The primary collimation material is a lead annulus 14.6 cm long with an inner diameter of 2.54

cm and an outer diameter of 9.5 cm. Both the inner and outer surfaces of the annulus are lined with 0.16 cm of tin to attenuate k-shell X-rays from the lead. The source itself is contained in a stainless steel button mounted on the head of a screw. This screw is affixed to a 4.4-cm plug which slides into the lead annulus. The first 1.9 cm of the plug near the source is brass while the rest is lead. With the source inside the holder, the opening angle of the radiation beam is  $23^\circ$ . This test was run for a variety of nuclear isotopes at a number of detector viewing angles [15].

For this test the detector response profiles were simulated as accurately as possible. This involved varying the thicknesses of volumes in the vicinity of the source to see how accurately these regions needed to be represented. Simulating these regions with millimeter accuracy or better proved necessary, since changes on this order caused significant effects in the observed energy deposition spectrum for most energies.

Fig. 3a through 3d illustrate the series of procedures used to reproduce an angular response profile observed by the LAD for  $\text{Cs}^{137}$  in the angular response test environment. Fig. 3a shows the 661 keV energy deposition spectrum for a LAD in the angular response test environment binned rather coarsely to highlight the off diagonal energy

deposition components. It is clear from this figure that the off diagonal components are important for accurate spectral deconvolution.

The first step in processing the LAD energy deposition spectrum to produce a detector response profile is to apply the radial response correction to the data. The radial response of the LADs refers to the property that the phototube light collection for an energy deposition at the edge of the crystal is about 85% of the light collection for the same energy deposition at the center of the crystal. This behavior has been measured in the radial response test for each detector [15]. In this test sources strongly collimated by lead shielding were placed at the surface of the CPD at different radial distances from the center of the detector crystal. Due to the tight collimation, an area on the detectors only a few centimeters in diameter was exposed at each source location. Each exposure produced Gaussian shaped photopeaks. The positions for the photopeaks of each source at each radial location were calculated and a quadratic fit to photopeak position vs. radial source location was calculated for each detector. This radial response function was applied to the simulated energy deposition spectrum to produce the radial response corrected spectrum shown in Fig. 3b. The radial response

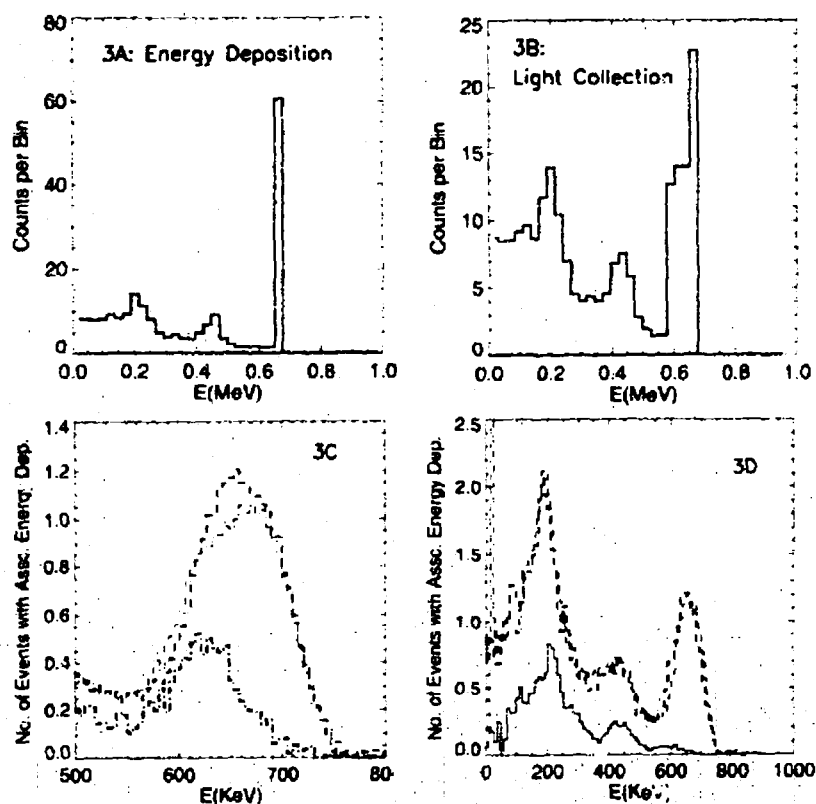


Fig. 3. Construction of detector response profiles for  $\text{Cs}^{137}$ . (a) simulated energy deposition (b) energy deposition convolved with radial response. (c) two detector response photopeaks at  $0^\circ$  incidence and a photopeak at  $90^\circ$  incidence  $\times 3$ . (d) comparison of simulated response (upper solid histogram) and measured response (dashed histogram). Also shown is the contribution to the response from the test environment (lower solid histogram).

functions differed between detectors as can be seen in the comparison of detector 1 (thin dotted histogram) and detector 3 (thin dashed histogram)  $\text{Cs}^{137}$  normal incidence photopeaks shown in Fig. 3c. The photopeaks here have markedly different shapes although their integrated amplitudes agree to within 0.5%. Also shown in the figure is the  $\text{Cs}^{137}$  photopeak response for detector 3 (thick dashed histogram) at  $90^\circ$  angle of incidence (multiplied by a factor of 3). In this case the photons are generally depositing their energy at the edge of the detector crystal so the photopeak response is at the low end of the radial response function and can be fit with a Gaussian line. Each detector's unique radial response function was used in the construction of its DRM.

Finally, the energy dependent detector resolution was folded through the energy deposition spectrum, corrected for radial response, to produce a detector response profile as shown in Fig. 3d. Here the higher solid histogram is simulation data for the angular response geometry and the dotted line is data from the angular response test for detector 3. The lower solid histogram is the component of the simulation results due to photons that scattered in the source holder and, to a lesser extent, in the test room geometry. The peak around 225 keV is partly due to photons back scattering off the source holder material

directly behind the source into the detector crystal and partly due to photons scattering off the quartz window behind the detector back into the crystal. Obviously only the latter component is appropriate for the DRMs in spacecraft configuration. The peak around 450 keV is due to photons scattering between  $45^\circ$  and  $60^\circ$  in the source collimator as well as photons that scatter in the detector crystal at nearly  $180^\circ$  then leave the crystal depositing only part of their energy. It is clear from this figure that accurate modeling of the source holder is important for an accurate understanding of the detector test results.

Fig. 4a–4d show the LAD response to the  $\gamma$ -ray lines of  $\text{Ba}^{133}$  at four representative source viewing angles. The  $\gamma$ -ray line energies and relative weights are: 382 keV at 8%, 356 keV at 69%, 302 keV at 14%, 276 keV at 7%, 80 keV at 36%, and 32 keV at 100%. These figures have the same format as Fig. 3d. At  $0^\circ$  there is little scattering from the test environment as demonstrated by the sparsely populated lower histogram. The plots show that the angular response of the LADs has a strong energy dependence. At large incident angles the environment within 3 or 4 m of the detector becomes important again for low energy photons. Here the detector is facing away from the source and the low energy photons from the beam have reasonably significant cross sections for Compton scattering off ob-

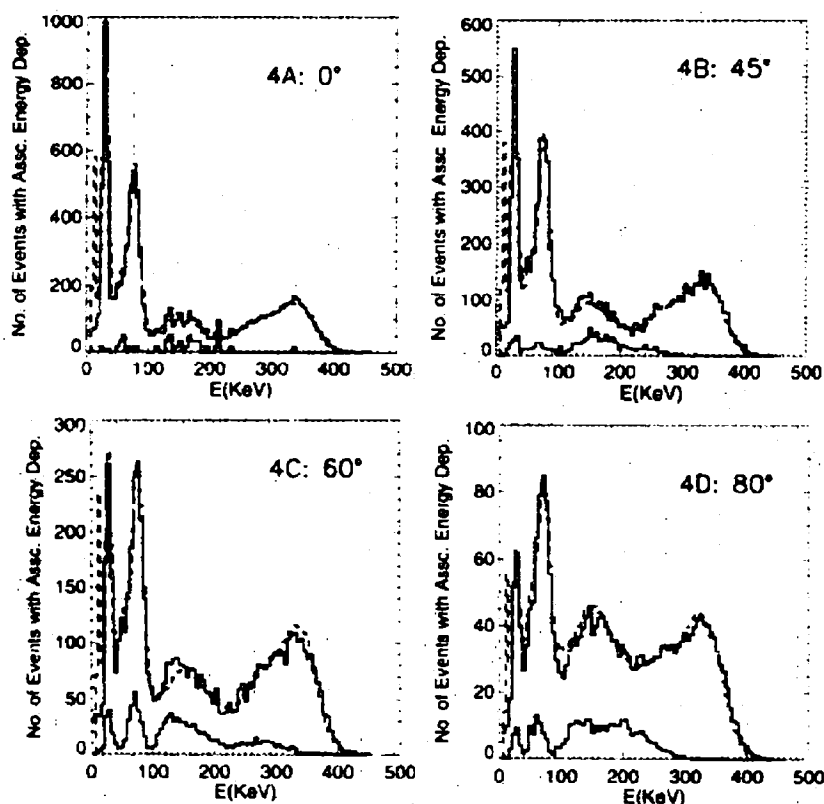


Fig. 4. Comparison between simulated response (upper solid histograms) and measured response (dashed histograms) for  $\text{Ba}^{133}$  for LADs at various angles of incidence. Also shown are the contributions to the response from the test environment (lower solid histograms).

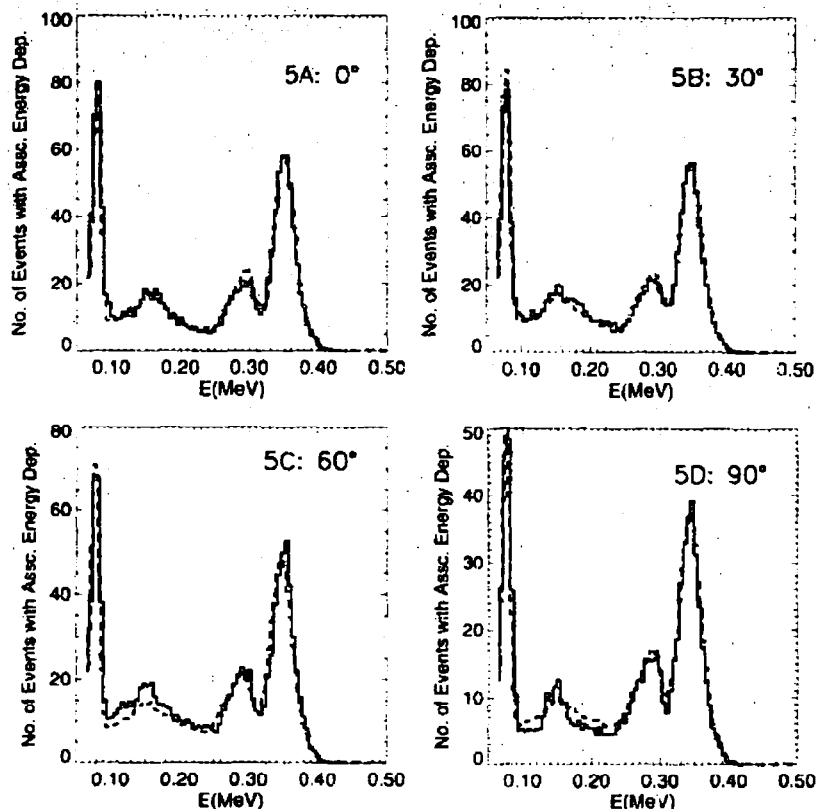


Fig. 5. Comparison between simulated response (solid histograms) and measured response (dashed histograms) for  $\text{Ba}^{133}$  for SDs at various angles of incidence.

jects in the vicinity of the detector. Also low energy photon attenuation is very sensitive to the thicknesses of the rings of material used to approximate the detector edge geometry. The geometry code used here did not have the sophistication to simulate either the local test environment or the detector edge geometry with high precision so precise amplitude of the low-energy large-angle LAD response is somewhat under-determined in this case. This

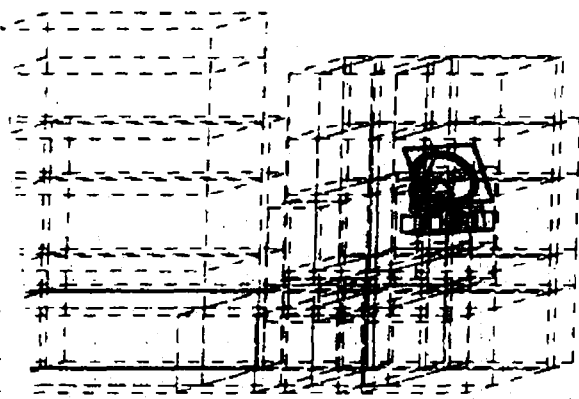


Fig. 6. The BATSE geometry imbedded in the GRO environment for the simulations of the DRMs used for data analysis of flight data.

region of the response was optimized using solar flare data obtained after launch [14]. An ensemble of solar flare measurements (where the sun's angle to each detector was known) were used to build a set of optimized low energy large angle response coefficients. The solar flare analysis verified that the high energy angular response was adequately determined with the angular response test data.

Fig. 5a–5d show the  $\text{Ba}^{133}$  response for the spectroscopy detectors at four source viewing angles. These plots show the superior energy resolution of the spectroscopy detectors as well as an angular response that is less dramatic than the LADs. Since the spectroscopy detectors have significant response at large angles, it is important to model the volumes of mass within 0.5 m of these detectors with precision. This will be discussed in more detail below.

The DRMs for in flight data analysis were created with a geometry that used the detector module placed on the corner of a fairly crude representation of the spacecraft geometry as shown in Fig. 6. The spacecraft simulation was derived from data collected during the mass model project [15]. The rectangular volumes employed contained the spacecraft mass to a precision of about 8 cm. There is also thermal blanketing surrounding the batse modules. The front face of the BATSE modules are covered by 0.07

gm/cm<sup>2</sup> of aluminized mylar. In this configuration the detector response profiles contain only the components appropriate for in-flight operation.

#### 4. The flexible data storage formats and DRM realization software

The simulation software was run for 66 energies between 10 keV and 100 MeV for the LADs and 71 energies

between 3 keV and 100 MeV for the SDs. The energies were selected to adequately sample regions where the response was changing quickly with energy, particularly around the NaI k-edge. One hundred thousand events were run for 10 viewing angles between 0° and 95° at each energy using a total of 2500 h of CPU time on VAXstation 3100 workstations. The energy deposition spectra from these simulations were stored in compressed form. These spectra were then processed into detector response profiles

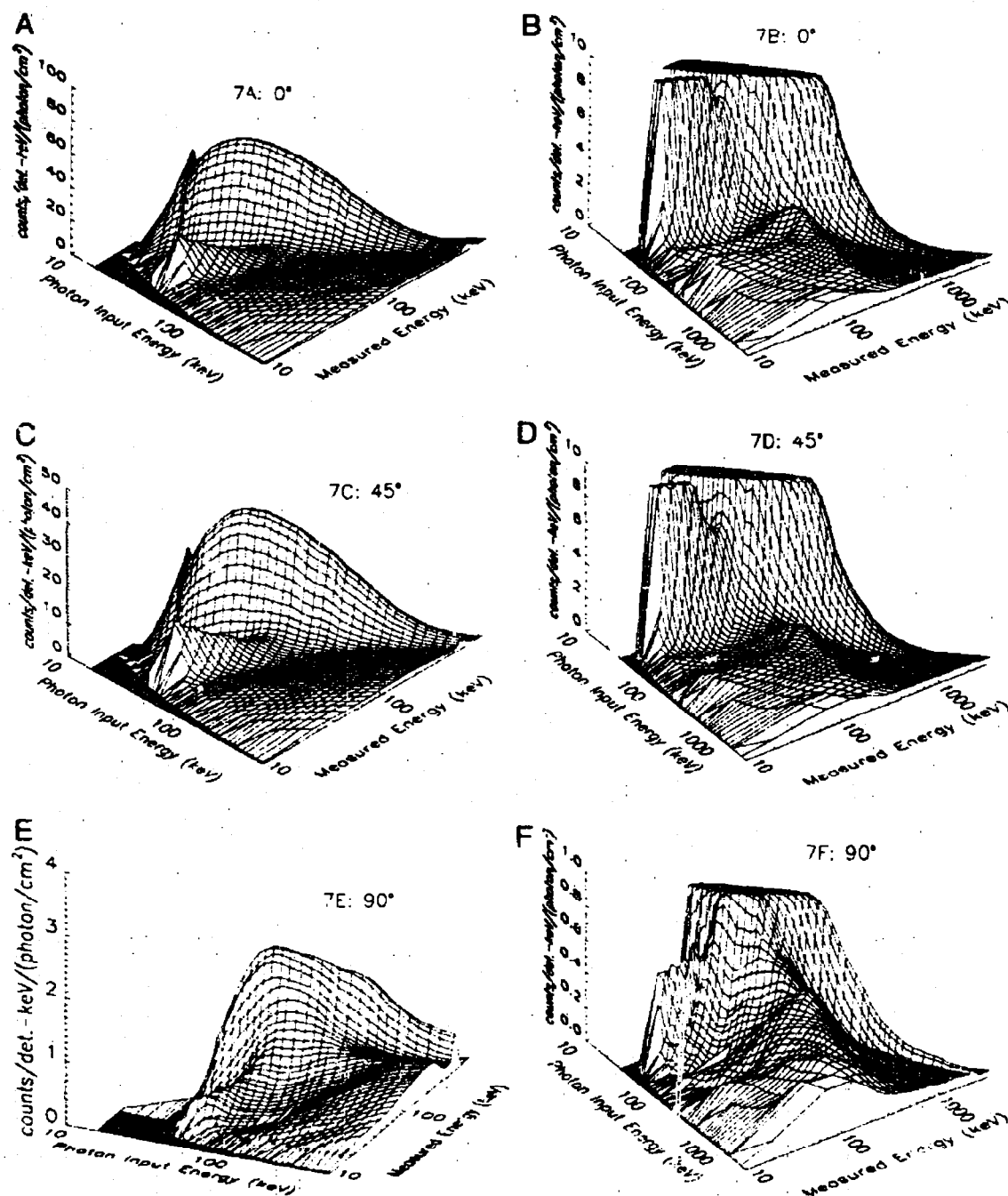


Fig. 7. Surface plots of LAD DRMs at various angles and energies.



by a separate piece of Fortran software. These detector response profiles were stored in 64 energy bins spaced from  $E = 0$  to  $E = 1.422$  times the photopeak energy.

The 64 bins in the detector response profiles for a particular energy were then parameterized as a function of detector zenith angle.

The functional form used for the LADs was

$$f(\theta) = A + B \cos(\theta^2 + 15^\circ) + C [\cos(\theta^2 + 15^\circ)]^2 + D [\cos(\theta^2 + 15^\circ)]^3 \quad (1)$$

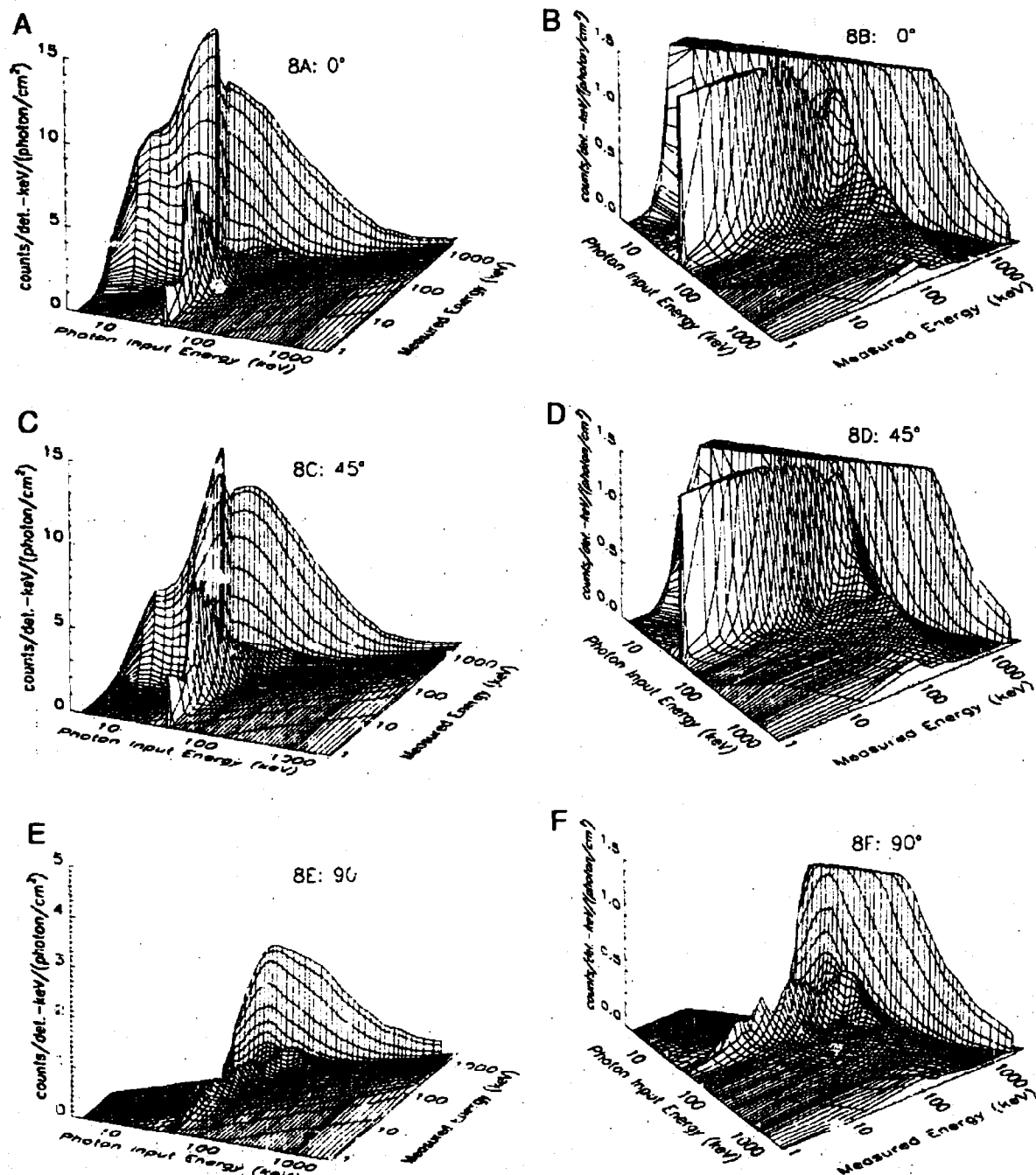


Fig. 6. Surface plots of SD DRMs at various angles and energies.

and for the SDs,

$$f(\theta) = A + B \cos(\theta + 15^\circ) - C[\cos(\theta + 15^\circ)]^2 + D[\cos(\theta + 15^\circ)]^3 \quad (2)$$

These functional forms were chosen to match the response as accurately as possible in the 50–300 keV BATSE burst trigger energy range. Given the flexibility of the functional form, the fit vs. angle is well within the statistics of the Monte Carlo simulation. The detector response data are stored at various stages in the processing in order to facilitate reprocessing at any time in order to incorporate any changes in detector performance or requested changes in the matrix representation.

The matrices are stored in a data structure that is accessed by data analysis software primarily through the configuration controlled subroutine response matrix. A scientist with programming resources simply inputs the detector number, the energy edges, and the source location into this subroutine and it passes back the appropriate DRM.

In particular, this algorithm will calculate a response matrix for matrices with many narrow input energy bins and whatever output binning the user selects, usually an output binning appropriate for a particular BATSE data type. Fine input energy binning can be important for accurate spectral fitting when the incident photon spectrum changes significantly across a data bin. For a given set of input bin edges the matrix integrator software finds the compressed matrix vectors whose input energies span the input bin edges including those vectors just outside the bin. The algorithm then interpolates between the compressed matrix vectors to points linearly spaced across the input bin range. The interpolation takes place in the compressed format so that the photopeak width and height are accurately calculated (Fig. 9 shows a portion of a SD matrix in compressed form.). These interpolated vectors are decompressed into output energy format for binning in the output energy dimension of the matrix. In general members of the BATSE science team use the input binning set at one third

the detector resolution at a particular energy. Finer binning may be important for spectra that change very rapidly with energy. The response matrix subroutine is accessed through the DRM\_GEN software available for spectral analysis at the GROSSC for those who wish to use fully developed data analysis algorithms.

## 5. Detector response matrix characteristics

The detector response matrices constructed using the spacecraft geometry are shown in Figs. 7a–8f. Fig. 7 plots show the LAD matrices for various angles between the source direction and detector normal. Fig. 7a shows the LAD DRM from 10 to 500 keV. The most prominent characteristic visible here is the NaI K-edge effect. Right above the K-edge the photopeak response drops discontinuously. This effect is not very noticeable in the actual LAD data because the relatively broad energy resolution smears out the abruptness of this effect. At somewhat higher input energies a secondary response peak appears below the main photopeak that gradually merges with the main photopeak around 100 keV. This secondary response peak is due to events where the photon re-emitted after the K-edge absorption escapes the crystal and it is important particularly for deconvolving low-energy spectra where the low energy photopeak and the secondary K-edge response peak contribute with similar strengths.

Fig. 7b shows the detail of the higher energy off-diagonal components of the LAD detector response matrix. Here the response has been truncated at an effective area of 10 cm<sup>2</sup> per keV. The off-diagonal response has two primary components here. One is the response below 250 keV due primarily to photons scattering of the LAD quartz window back into the NaI. These photons are generally distributed below the Compton backscatter limit energy of half the electron rest mass although there is a response enhancement just below this limit. The other off-diagonal component is a weak secondary response peak that follows the main response peak at an energy half the electron rest mass below the photopeak energy. This component is primarily due to photons that bounce backward right out of the LAD crystal depositing all but the recoil photon energy. This effect is strongest for source viewing angles of 0° due to the disk shape of the LAD crystal. Fig. 7b, 7d, and 7f show this component weakening compared to the other off diagonal component as a function of source viewing angle.

Fig. 7c shows that the LAD photopeak response at 45° peaks at about half the response at 0°. This peak is at lower energies so both the NaI crystal viewing angle and attenuation in the CPD play a role here. Fig. 7e shows the peak response down by a factor of 20 with significant attenuation at low energies. The matrix has large off-diagonal components that make it ill-conditioned for spectral inversion.

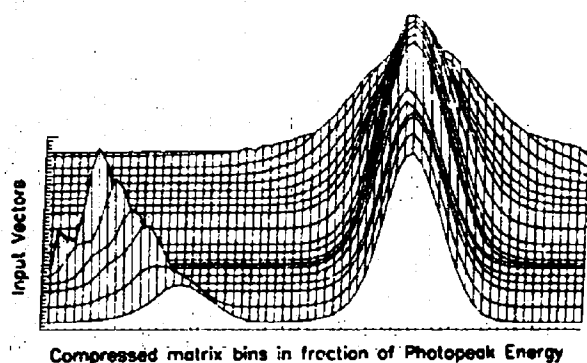


Fig. 9. Surface plot of compressed SD DRM at low energies showing post K-edge shift.

Fig. 8a-8f show the SD DRMs in the same format as in Fig. 7. The K-edge effect here is similar to that in the LADs seen in Fig. 8a. However, the SD resolution is narrow enough that the jump in photopeak intensity is noticeable in the SD counts spectra. Also these detectors have a knee in their sensitivity between 8 and 12 keV due to the beryllium window on the front face of the detector. Fig. 8b shows that the contribution to the off-diagonal matrix component from photons that bounce directly out of the crystal is small compared to the LADs. This is expected due to the differences in the LAD and SD geometries. The off diagonal components below 250 keV here are largely due to scattering off the BATSE module material around the spacecraft. In fact the SD detector effective area exceeds the total face on geometric area above 50 keV due to photons scattering into the detector from material around the detector. For this reason the material around the spec detector must be simulated with precision.

Fig. 8f shows that at large angles the low-energy response of the SD detectors is severely attenuated. There is little photopeak response below 50 keV. The differences between the SD face-on and edge-on response is due to the different window thicknesses on the front and sides of the detector. There is more than four times as much absorber around the sides of the SD detectors than there is on the front face. Also photons generally hit the cylindrical surface of the detector side at an angle to the surface normal so the actual path length through the outer material is greater than its radial thickness. Since the low-energy response results from photons passing through the detector face, it is nearly proportional to the inverse cosine of the source viewing angle.

Fig. 9 shows the low-energy part of a face-on SD matrix presented in compressed form. In this format, the photopeaks are all lined up in the same bin. This results in smoother interpolations between input energies. The important feature here is the abrupt drop in the photopeak response at the NaI K-edge. Also included in these matrices is a 1.27% shift in the photopeak centroid due to decreased scintillator light output right above the K-edge, in the energy range 34 to 38 keV. This shift can be seen in Fig. 9, however it is much smaller than the detector resolution so its impact on observed counts spectra will be heavily masked.

## 6. Summary

These DRMs are valuable tools that are used for the analysis of large quantities of astrophysical data. The range of energies and source viewing angles over which they are calculated is necessary to address all the data analysis conditions of interest with this astrophysical instrument. The production of the DRMs relies strongly on algorithmic problem solving techniques.

The computer tools that allow for the construction and use of these types of tools have only become available in the last 5 to 10 years and already there are new machines that are available for the same cost as the ones used to produce these DRMs that are an order of magnitude more powerful. With these newer computing facilities, it is now possible for the accuracy of the geometric modeling and the practical complexity of the on-line data analysis algorithms to increase significantly over the next decade.

## References

- [1] G. Fishman et al., Proc. GRO Science Workshop, ed. N. Johnson, (2)39-(2)50 (1989).
- [2] G. Fishman et al., Proc. GRO Science Workshop, ed. N. Johnson, (3)47-(3)62 (1989).
- [3] J. Higdon et al., ARA&R 28 (1990) 401.
- [4] B. Harmon et al., Proc. Compton Observatory Science Workshop, eds. R. Shrader, N. Gehrels and B. Dennis (1992) p. 315.
- [5] R. Wilson et al., Proc. Compton Observatory Science Workshop, eds. M. Friedlander, N. Gehrels and D. Macomb (1992) p. 69.
- [6] A. Aschwanden et al., Astrophys. J. 417 (1993) 790.
- [7] G. Fishman et al., Science 264 (1994) 1313.
- [8] G. Pendleton et al., to be published in Astrophys. J.
- [9] R. Ford et al., Stanford-U-SLAC-210 (1978).
- [10] R. Ford et al., Stanford U-SLAC-265 (1985).
- [11] E. Browne et al., in Table of Isotopes, eds. M. Lederer and V.S. Shirley (Wiley, New York, 1978).
- [12] G. Pendleton et al., Proc. GRO Science Workshop, ed. N. Johnson, (4)547-(4)553 (1989).
- [13] G. Pendleton et al., Proc. Compton Observatory Science Workshop, eds. R. Shrader, N. Gehrels and B. Dennis (1992) p. 47.
- [14] G. Pendleton et al., Proc. Gamma-Ray Burst Workshop, eds. W. Paciesas and G. Fishman (1992) p. 395.
- [15] J. Horack, NASA Reference Publication 1268, 1991.